Metal-support interface engineering for stable and enhanced hydrogen evolution reaction

Jinhua Mai [a], Yulong Zhang [g], Huan He [a], Yue Luo [a], Xiaoqun Zhou [e], Kunsong Hu [a], Gang Liu [f], Manoj Krishna Sugumar [c], Chee Tong John Low [c], Xinhua Liu [d], Rui Tan [b,c,*]

[a] School of Resources, Environment and Materials, Guangxi University, Nanning, 530004, China
[b] Department of Chemical Engineering, Swansea University, Swansea, SA1 8EN, UK
[c] Energy Innovation Centre, Warwick Manufacture Group, University of Warwick, Coventry, CV4 7AL, UK
[d] School of Transportation Science and Engineering, Beihang University, Beijing, 100191, China
[e] School of Environment, Harbin Institute of Technology, Harbin, 150090, China
[f] IDTECH (Suzhou) Co.,Ltd Suzhou, 215217, China
[g] College of Mechatronical and Electrical Engineering, Hebei Agricultural University, Baoding, China

ARTICLE INFO

ABSTRACT

Hydrogen has emerged as a green and sustainable pathway towards achieving global decarbonization and net-zero emissions, intensely driving the need for efficient hydrogen production protocols. Electrocatalytic hydrogen evolution reaction (HER) holds great potential as a scalable, eco-friendly and safe avenue for efficient hydrogen production. However, the large-scale implementation of electrocatalytic HER is substantially challenged by the high-cost and unstable materials that are mainly fabricated from noble metals, e.g., Pt and Pd. Given this challenge, we adopted an interface engineering strategy to immobilize nanoscale Pt particles within the framework of nitrogen-doped CNTs, namely Pt@N-CNTs, where electronic metal-support interaction (EMSI) plays an important role in enabling orbital rehybridization and regulating the charge transfer through the metal-support interface, thereby considerably improving the electrocatalytic activity. With limited content of noble metals, our developed Pt@N-CNTs delivered superior HER performance with an ultralow overpotential of 5.8 mV at 10 mA cm^{-2} and demonstrated a high mass activity of 12.72 A mg$_{Pt}^{-1}$ at an overpotential of 50 mV as well as excellent stability under harsh acidic conditions. At 500 mA cm^{-2}, Pt@N-CNTs surprisingly exhibited an overpotential of 55.2 mV, outperforming that of commercial 20 wt% Pt/C catalysts (131.5 mV). Importantly, we established a straightforward, scalable, and time-saving microwave reduction strategy, alluding to its promising commercial viability. This work therefore sheds light on the development of high-performance electrocatalysts for hydrogen evolution and water electrolysis.

1. Introduction

Hydrogen is widely regarded as a viable alternative to traditional chemical fuels due to its high energy density, cleanliness and sustainability [1,2]. Water electrolysis, as a net-zero emission process, is among the various methods used for hydrogen production, enabling efficient and sustainable production [3,4]. Catalysts play a crucial role in the cathodic hydrogen evolution reaction (HER) for hydrogen production through water electrolysis. However, the large-scale deployment of cathodic hydrogen evolution reactors is highly limited by the performance of current catalysts [5,6]. Addressing this challenge necessitates novel material solutions and engineering strategies for the development of efficient and economically viable catalysts [7–9].

Platinum (Pt) is the most efficient HER catalyst due to its near-zero hydrogen adsorption free energy [10–12]. However, its scarcity and high cost pose significant limitations to its widespread application in this field [13,14]. Considerable research efforts have been devoted to developing non-noble metal catalysts as viable alternatives towards Pt-based catalysts in order to achieve high activity and stability, e.g., transition metal nitrides [15–17], sulfides [18–20] and phosphides [21–23]. Though various families of non-noble metal catalysts have been proposed, none can compete with the overall performance of the state-of-the-art Pt catalyst. Reducing the Pt loading while maintaining the catalytic activity therefore receives more research attention. As a

prototypical approach, active Pt is expected to distribute within a given catalyst in a single-atom scale so that the catalytic activity can be maximized whilst sustaining a low Pt loading. Zhou et al. demonstrated this phenomenon by immobilizing single-atom Pt onto a two-dimensional NiO/Ni heterostructure nanosheet, which was subsequently attached to an Ag nanowire conductive network [24]. Their findings delivered excellent HER performance, strongly evidenced by a mass activity of 20.6 A mg^{-1} Pt at an overpotential of 100 mV. Wang et al. anchored single-atom Pt on a cobalt sulfide supports to create a composite material and demonstrated that it had an overpotential of only 28 mV at a current density of 10 mA cm^{-2} [25]. Despite notable advancements, fabricating single-atom Pt catalysts generally requires sophisticated processing methods and the developed catalysts possess limited loading of active sites, which barely meet the demands of extensive commercialization [26–28]. A rational and strategic design is highly needed to develop useable Pt catalyst, ensuring optimal loading, enhanced efficiency and cost-effectiveness.

Electronic metal-support interaction (EMSI) plays an important role in designing advanced catalysts by allowing the tuning of the electronic structure and d-band center of the loaded ultrafine nanoparticles (NPs), as well as optimizing the reduction of intermediates [29]. NPs demonstrate size effects in catalytic processes due to the high proportion of low-coordination atoms, high-coordination atoms and strong binding energy between metals and reactants [30,31]. When the size decreases, an increase in exposed active sites and interfacial sites occurs, resulting in an enhanced EMSI effect [32,33]. Furthermore, the EMSI effect is strongly influenced by the morphology of NPs and the carbon substrates where suitable carbon supports not only serve as physical supports, but also impact the geometric configuration and electronic structure of the supported metal, thereby promoting catalytic activity [34,35]. Carbon nanotubes (CNTs) are considered as valuable carbon supports due to their ability to function as active sites for HER, achieved by modulating electron spin density and charge redistribution through supported transition metals [36]. However, the weak interaction between the supported metal and undoped carbon support often results in metal aggregation and diminishes the catalytical activity [37], for which the issue can be mitigated by introducing nitrogen into CNT substrates to enhances the EMSI effect and stabilize NPs [38]. Nonetheless, developing viable catalysts that combine these aforementioned strategies present a critical challenge in the design and synthesis methodology.

Herein, we reported a one-step microwave-assisted approach to immobilizing ultrafine Pt NPs on aniline-stacked carbon nanotubes, namely Pt@N-CNTs, and maximizing EMSI effect to achieve efficient HER at large current density via engineering the metal-support interface (Fig. 1 and Fig. S1). Specifically, ultrafine Pt NPs are uniformly embedded within the highly electronic-conductive carbon framework that was established by hollow tubular CNTs. Interestingly, nitrogen atoms derived from aniline groups can further enhance the interface contact between metal and support atoms, thereby effectively enhancing the stability of the Pt NPs. Despite limited loading of Pt NPs, our developed Pt@N-CNTs delivered an ultra-low overpotential of 55.2 mV at an industrial-grade large current density of 500 mA cm^{-2}, which was significantly lower than that of commercial Pt/C catalysts with higher Pt loads, and demonstrated a high mass activity of 12.72 A mg$_{Pt}^{-1}$ at an overpotential of 50 mV. The Pt@N-CNTs catalyst was applied to the anode of an Mn–H$_2$ flow battery to achieve enhanced anode reaction kinetics. This work provides a reliable reference for developing cost-effective and efficient HER catalyst strategies for large-scale production and promotes the widespread application of sustainable energy technologies.

2. Experimental section

2.1. Materials

Aniline (C$_6$H$_7$N), ethylene glycol (C$_2$H$_6$O$_2$) and isopropyl alcohol (C$_3$H$_8$O) were purchased from Energy Chemical. Carbon nanotubes, produced by Xuzhou LanoXene Research Institute, consist of a single-walled carbon nanotube conductive slurry with 0.4 % carbon nanotubes and 0.6 % Carboxymethyl cellulose. They are used directly without any pretreatment. Chloroplatinic acid hexahydrate (H$_2$PtCl$_6$·6H$_2$O) was purchased from Shanghai Jiu Ling Chemical Co., Ltd. 5 wt% Nafion solution was afforded by DuPont. Commercial Pt/C (20 %) catalyst was bought from COTRUN NEW ENERGY.

2.2. Preparation of N-CNTs

To synthesize N-CNTs, 30 mL of a CNT slurry (containing 0.4 wt% CNTs) was thoroughly mixed with 6 mL of aniline. Following this, 100 mL of ultrapure water was added, and the mixture was stirred magnetically for 6 h to achieve a uniform dispersion. Subsequently, the dispersion was filtered to obtain a black, viscous substance. This substance was then uniformly dispersed in ultrapure water and filtered again. Multiple filtration cycles were repeated to eliminate excess
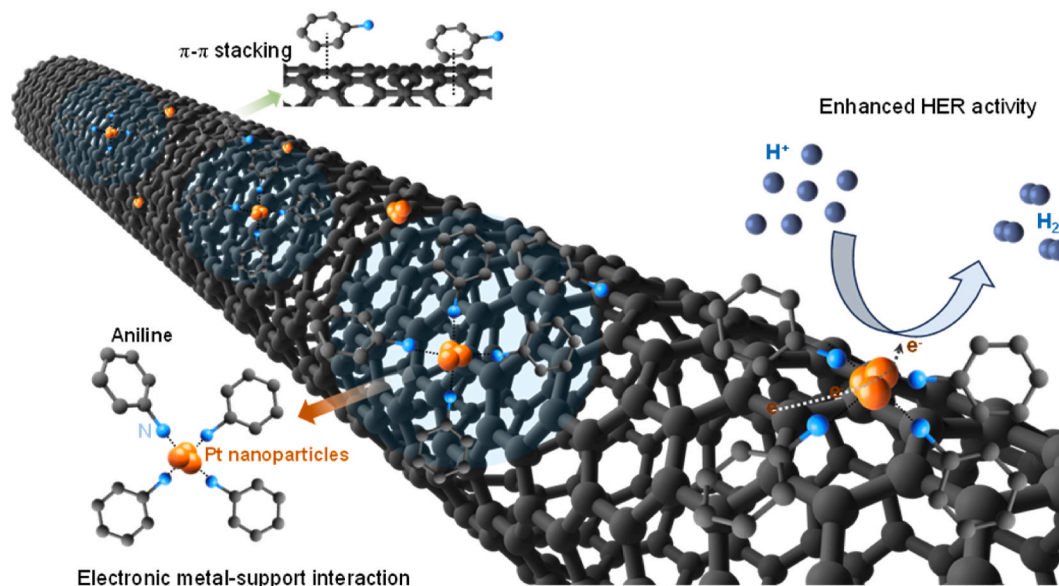

Fig. 1. Design principle of metal-support engineering to enhance electrocatalytic activity for hydrogen evolution.

aniline. Finally, the filtered product was dried overnight at 60 °C to obtain N-CNTs.

2.3. Preparation of Pt@N-CNTs

Pt@N-CNTs were synthesized using a microwave irradiation method. Initially, the prepared N-CNTs were dispersed in 100 mL of ultrapure water. Then, 2.4 mL of a H_2PtCl_6 solution with a concentration of 0.0965 mol L^{-1} was added to the dispersion, and the mixture was stirred for 4 h. Subsequently, the dispersion underwent repeated filtration and subsequent dispersion to remove unsupported $PtCl_6^{2-}$ ions. The resulting product was dried at 60 °C for 10 h. Afterward, 50 mL of ethylene glycol was added to the product and sonicated to achieve a uniform dispersion. The dispersion was subjected to a 2 min microwave reaction at 720 W, followed by cooling and repeated filtration. Finally, the product was dried overnight at 60 °C to obtain Pt@N-CNTs.

2.4. Material characterizations

Scanning electron microscopy (SEM, Hitachi SU8020) was employed to study the surface morphology of the samples, and the respective compositions were investigated by energy-dispersive X-ray spectroscopy (EDS). Transmission electron microscopy (TEM, FEI Titan G2 80–300) was performed to study the morphology and phase structure. The phase structure was analyzed by X-ray diffraction (XRD) using a diffractometer (SMARTLAB3KW) with Cu Ka radiation. FTIR spectroscopy was performed on an FT-IR Spectrometer Nicolet iS50. Inductively coupled plasma mass spectrometry (ICP-MS , Agilent ICPMS 7700) was utilized to determine the content of Pt. X-ray photoelectron spectroscopy (XPS) measurements were taken by the Thermo ESCALAB 250XI with a monochromatic Al Ka X-ray source.

2.5. Electrochemical measurements

The catalyst ink was prepared by mixing 5 mg of the catalyst, 20 μL of 5 wt% Nafion, and 0.98 mL of an isopropyl alcohol solution. After undergoing ultrasonic pulverization for 3 min, 8 μL of the ink was evenly dropped onto a polished glassy carbon electrode (GCE) with a diameter of 5 mm and an area of 0.19625 cm^{-2}. The GCE was then dried at room temperature. All electrochemical measurements were conducted using a CHI 760E electrochemical workstation (CH Instruments, China), with the GCE, graphite rod, and standard hydrogen electrode serving as the working, counter, and reference electrodes, respectively. A 1 M $HClO_4$ solution (H_2 saturated) was utilized as the electrolyte. CV measurements were carried out for over 50 cycles to achieve a steady state. Subsequently, CV measurements were performed in the non-Faradaic region at a scan rate ranging from 20 to 120 mV s^{-1}. LSV measurements were conducted in the electrolyte at a scan rate of 5 mV s^{-1} with iR compensation. EIS was performed with an open voltage and a 5 V amplitude across a frequency range from 10^5 to 0.01 Hz. The Mn–H_2 battery consisted of a Nafion 212 membrane and two graphite bipolar plates that are in contact with gold-plated copper current collectors. The current collectors are held together utilizing anodized aluminum end plates. The positive electrode consists of carbon felt, and the active area of the electrode is 4 cm^2. The hydrogen negative electrode was purchased from Fuel Cell Store. Generated hydrogen was purged into the reaction cell with a flow rate of 100 mL/min. The electrolyte is an equimolar solution of 1 M $MnSO_4$ and 1 M $Ti(SO_4)_2$ in 3 M H_2SO_4 solution. To achieve discharge at different states of charge, the battery was operated for a defined time under fully charged electrolyte to reach 80 % state of charge.

3. Results and discussion

3.1. Preparation of Pt@N-CNTs catalysts

The Pt@N-CNTs composite was synthesized by anchoring Pt NPs onto the surface of CNTs along with aniline molecules, followed by reduction through microwave-assisted reactions. Through the π-π stacking, aniline molecules can readily stack onto the surface of CNT and effectively interact with CNTs during subsequent synthesis and electrocatalytic processes [39,40]. Thereafter, a solution of H_2PtCl_6 was added to the mixture of aniline molecules and CNTs. At pKa of ~4.6, Amine groups (-NH_2) of aniline undergo protonation to form –NH_3^+, thus introducing positive charges to aniline/CNT composites where $PtCl_6^{2-}$ ions can be immobilized on the CNT surface through this electrostatic interaction. Through microwave irradiation with the use of ethylene glycol as a reducing agent, $PtCl_6^{2-}$ is reduced to ultrafine Pt NPs depositing on the surface of aniline/CNT composites, namely Pt@N-CNTs. Aniline/CNT composites were treated throughout identical processes to obtain the reference samples, namely N-CNTs. The Pt@N-CNTs catalyst prepared in this manner effectively avoids the agglomeration of Pt NPs, and is anticipated to exhibit a robust EMSI and enhanced HER activity.

Fourier-transform infrared spectroscopy (FTIR) was employed to verify the presence of aniline in N-CNTs. Prior to the tests, samples were thoroughly washed by deionized water to remove the free aniline molecules. The FTIR spectrum exhibits absorption peaks at 1578 and 1496 cm^{-1}, which correspond to the stretching vibration of N–H bonds (Fig. 2a). Peaks at 1292 and 1227 cm^{-1} attribute to the stretching vibration of C–N bonds, whereas peaks at 1123 and 830 cm^{-1} originate from the bending vibration of C–H bonds. The positions of these peaks confirm the successful immobilization of aniline on the surface of N-CNTs. X-ray photoelectron spectroscopy (XPS), as shown in Fig. 2b and S3, confirms the presence of only carbon (C), nitrogen (N), and oxygen (O) in N-CNTs without detectable impurities. The C 1s spectrum reveals the presence of sp^2-hybridized carbon atoms, indicating a low concentration of defects in the CNTs. Additionally, the low I_D/I_G also indicated low defect of N-CNTs (Fig. S4). The trace amount of nitrogen observed in the carbon matrix can be attributed to the –NH_2 groups of the immobilized anilines. The O 1s peak at 532.4 eV may originate from Carboxymethyl cellulose or adsorbed H_2O. The morphology of Pt@N-CNTs was further investigated using transmission electron microscopy (TEM). In comparison to the N-CNTs (Fig. 2d–e, S2), Pt@N-CNTs displays a uniform distribution of Pt NPs on the N-CNTs substrate while preserving the structural integrity of the CNTs. Therefore, these results confirmed the successful preparation of Pt@N-CNTs catalysts.

3.2. Structural characterization and metal-support interfacial interaction

The Pt-dispersion and crystalline structure of our developed catalysts was unveiled by high-resolution TEM (HRTEM) and X-ray diffraction. HRTEM clearly demonstrate the Pt NPs are well dispersed and embedded in the carbon framework that was created by aniline/CNT composites (Fig. 2f and g). In addition to well-dispersed Pt NPs with an average diameter of 2.15 nm, lattice fringes exhibiting a spacing of 0.198 nm corresponding to the (200) crystal plane of Pt are observable (Fig. 2c–h). Fast Fourier transform (FFT) pattern (Fig. 2i) confirms the cubic structure of the Pt NPs in Pt@N-CNTs. Furthermore, energy dispersive X-ray spectroscopy (EDS) mapping (Fig. S5) demonstrates the homogeneous distribution of C, N and Pt elements on the CNT substrate of Pt@N-CNTs. The crystalline structure was further investigated using XRD. As shown in Fig. 3a, the diffraction peaks at 39.8°, 44.8°, 67.5° and 80.6° correspond well to the (111), (200), (220) and (311) planes of the face-centered Pt crystal (PDF#04–0802), indicating the successful reduction of Pt on the N-CNTs surface. The diffraction peak at 2θ = 23° can be attributed to the characteristic peak of carbon graphitization in CNTs. The XRD spectrum exhibits a sharp peak for Pt(111), suggesting a
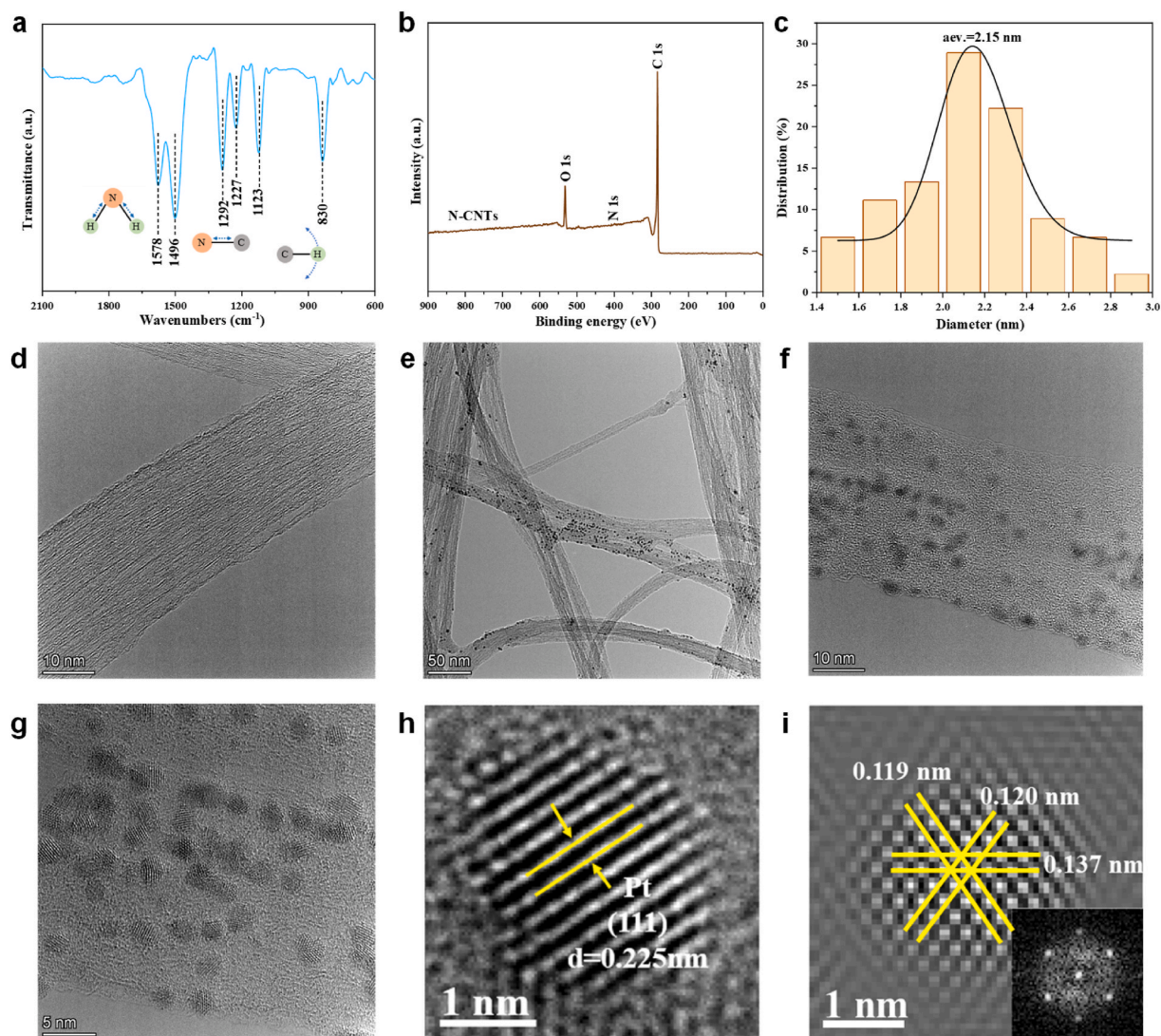
Fig. 2. Characterization of Pt@N-CNTs catalyst. **a.** FTIR spectroscopy of N-CNTs. **b.** XPS spectra of N-CNTs. **c.** Corresponding particle size distribution of the Pt NPs. **d.** TEM images of N-CNTs. **e.** TEM images of Pt@N-CNTs. **f-g.** HRTEM images of Pt@N-CNTs. **h-i.** FFT patterns.

high degree of crystallinity of the Pt NPs present in the catalyst. Importantly, the lack of overlapping sharp peaks indicates a homogeneous distribution of the Pt NPs. Compared to the XRD patterns of CNTs and N-CNTs, the XRD pattern of Pt@N-CNTs retains the characteristic peaks of carbon graphitization seen in CNTs and additionally exhibits characteristic peaks of Pt. This indicates the successful loading of Pt on the N-CNTs.

The detailed elemental composition and metal-support interfacial interaction was investigated by XPS analysis. Though N-CNTs and Pt@N-CNTs, they have identical spectra, trace amount of Pt was detected in Pt@N-CNTs (Fig. 3c), suggesting that the N-CNTs supports are mechanically and electrochemically stable over the reduction process of Pt. Notably, chlorides that are detrimental to the Pt-catalyst stability, were not evidenced in the XPS spectra, indicating complete dechlorination after the application of microwave treatment. The high-resolution N 1s spectrum can be separated into four distinct components with binding energies of 398.4, 399.4, 400.6, and 402.5 eV, representing the peaks of pyridinic N (Py-N), pyrrolic N (Pr–N), graphitic N (G-N), and oxidized N (O–N), respectively (Fig. 3b). The content of N is calculated to be 1.24 at%. In the Pt 4f spectrum (Fig. 3d), it is observed that the binding energy of Pt at 71.58 eV is close to that of Pt^0 (71.1 eV), albeit with a slight positive shift. Notably, the characteristic peak of Pt@N-CNTs is shifted to a higher energy compared to 20 wt% Pt/C,

indicating a greater electron depletion and higher oxidation state of Pt atoms within the Pt@N-CNTs composite. The observed phenomenon can be attributed to the strong EMSI effect between the N-doped carbon support and the Pt NPs. Furthermore, it indicates a strong interaction between Pt and aniline, leading to the formation of $Pt^{\delta+}$. Additionally, the Pt loading in Pt@N-CNTs is verified to be approximately 8.18 wt% through the analysis conducted using inductively coupled plasma mass spectrometry (ICP-MS). These results clearly support the viability of engineering the interface between Pt NPs and N-CNT support. The enhanced electronic metal-support interaction can strongly immobilize the dispersed NPs whilst maintaining or maximizing their electrocatalytic activity.

3.3. Electrocatalytic performance evaluation

To investigate the influence of active loading on the electrocatalytic performance, a series of Pt@N-CNTs samples were prepared, and the Pt loadings were determined using ICP-MS (Fig. S8). Graphite rods were employed as counter electrodes to evaluate the HER activity of the different catalysts in H_2-saturated 1 M $HClO_4$ electrolyte. For comparison, **commercial 20 wt% Pt/C** was chosen as the benchmark for comparison, and all LSV curves were IR corrected (the uncorrected LSV curves are shown in Fig. S9). As shown in Fig. 4a, the Pt@N-CNTs
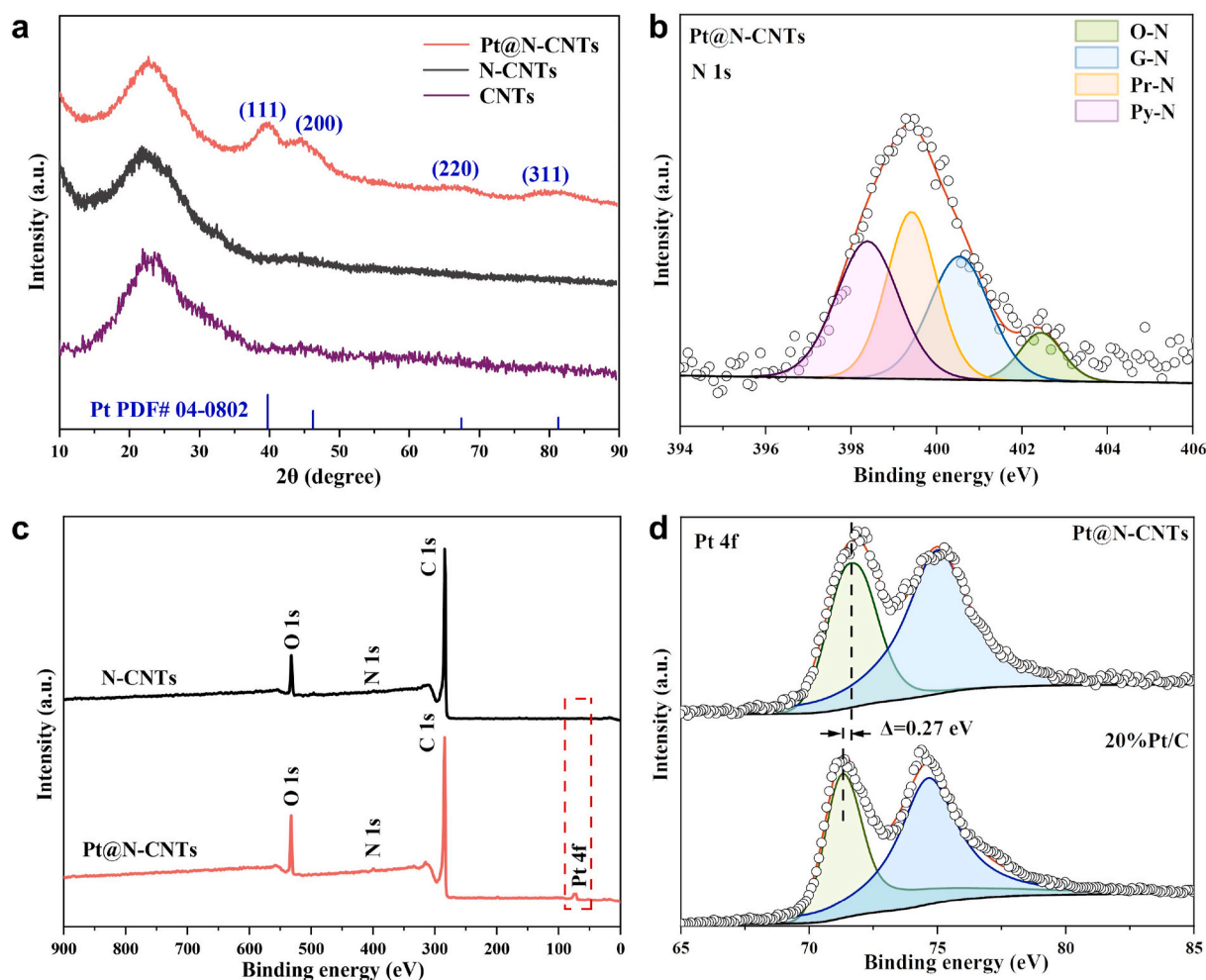
Fig. 3. Characterization of structures and metal-support interface. a. XRD pattern of CNTs, N-CNTs and Pt@N-CNTs. **b.** High-resolution N 1s spectra of Pt@N-CNTs. **c.** XPS spectra before and after loading Pt. **d.** High-resolution Pt 4f XPS spectra of the Pt@N-CNTs and 20 wt% Pt/C.

catalyst with Pt loading exhibits significantly enhanced HER activity compared to the pristine N-CNTs. Conversely, the Pt-free N-CNTs are inert towards HER, with a negligible current density. In comparison to the 20 wt% Pt/C catalyst, all the Pt@N-CNTs catalysts demonstrate better HER activity with low overpotentials (Fig. 4b). As a typical example, Pt@N-CNTs-8.18 catalyst with the lowest Pt loading exhibits an extremely low overpotential of only 11.7 mV at a current density of 10 mA cm^{-2}, surpassing the performance of the 20 wt% Pt/C catalyst (12.9 mV). Furthermore, the Pt@N-CNTs-16.18 catalyst achieves an even lower overpotential of 5.8 mV. To the best of our knowledge, Pt@N-CNTs exhibits a small overpotential at 10 mA cm^{-2}, indicating its high efficiency as an HER electrocatalyst compared to recently reported Pt-based HER catalysts (Fig. 4g and Table S4). Additionally, the Pt-CNTs catalyst without added aniline exhibited inferior performance, surpassing only that of N-CNTs. This suggests that the addition of aniline can enhance the HER performance of the Pt@N-CNTs catalyst. In terms of the operation at high currents, Pt@N-CNTs catalysts still maintain excellent HER activity. For instance, Pt@N-CNTs-8.18 demonstrates a lower overpotential than Pt/C catalyst at 500 mA cm^{-2} (125.4 and 131.5 mV, respectively). With a slight increase in the Pt loading to 9.89 wt%, the overpotential significantly decreases to 72.7 mV, and it further decreases to 55.2 mV at 16.18 wt%. The exceptional HER performance can be attributed to the strong electron-accepting ability of the nitrogen atom in aniline, which leads to a strong EMSI effect between the nitrogen-containing support material and the Pt NPs. Consequently, this strong interfacial interaction effectively impedes the migration and

aggregation of the Pt NPs, thereby maintaining a high dispersion even at high current densities.

To assess the kinetic behaviors and determine the HER mechanism of the catalysts, the Tafel slope is calculated (Fig. 4c and S11). Pt@N-CNTs catalysts exhibit significantly lower Tafel slopes (e.g., Pt@N-CNTs-16.18: *ca.* 16.20 mV dec^{-1}) compared that of Pt/C catalyst (34.75 mV dec^{-1}), indicating a typical Tafel mechanism for HER. The lower Tafel slope implies a faster increase in current density and a lower potential for the catalyst, suggesting its greater practical value. By analyzing the Tafel diagram (Table S2), the exchange current density of Pt@N-CNTs-16.18 is calculated to be 7.95 mA cm^{-2}, which is higher than that of Pt/C (5.71 mA cm^{-2}). This further confirms the improved electrocatalytic activity of Pt@N-CNTs.

Additionally, the electrochemically active surface area (ECSA) can elucidate the physical nature of various catalytic activities, which can be determined by the double-layer capacitance (Cdl) via cyclic voltammetry (CV). As depicted in Fig. 4e and S10, the CV curves taken between 0.1 and 0.2 V at scan rates ranging from 20 to 120 mV s^{-1} demonstrate that, except for Pt@N-CNTs-8.8, all samples exhibit higher capacitance compared to Pt/C catalyst (3.87 mF cm^{-2}), with Pt@N-CNTs-16.18 achieving an impressive value of 8.08 mF cm^{-2}. The corresponding ECSA values are provided in Table S3. The higher Cdl of Pt@N-CNTs indicates that it possesses more active sites to facilitate catalytic reactions. This can be attributed to the highly dispersed ultrafine Pt NPs on the hollow tubular structure with a larger surface area of CNTs. Electrochemical impedance spectroscopy (EIS) is a valuable technique for
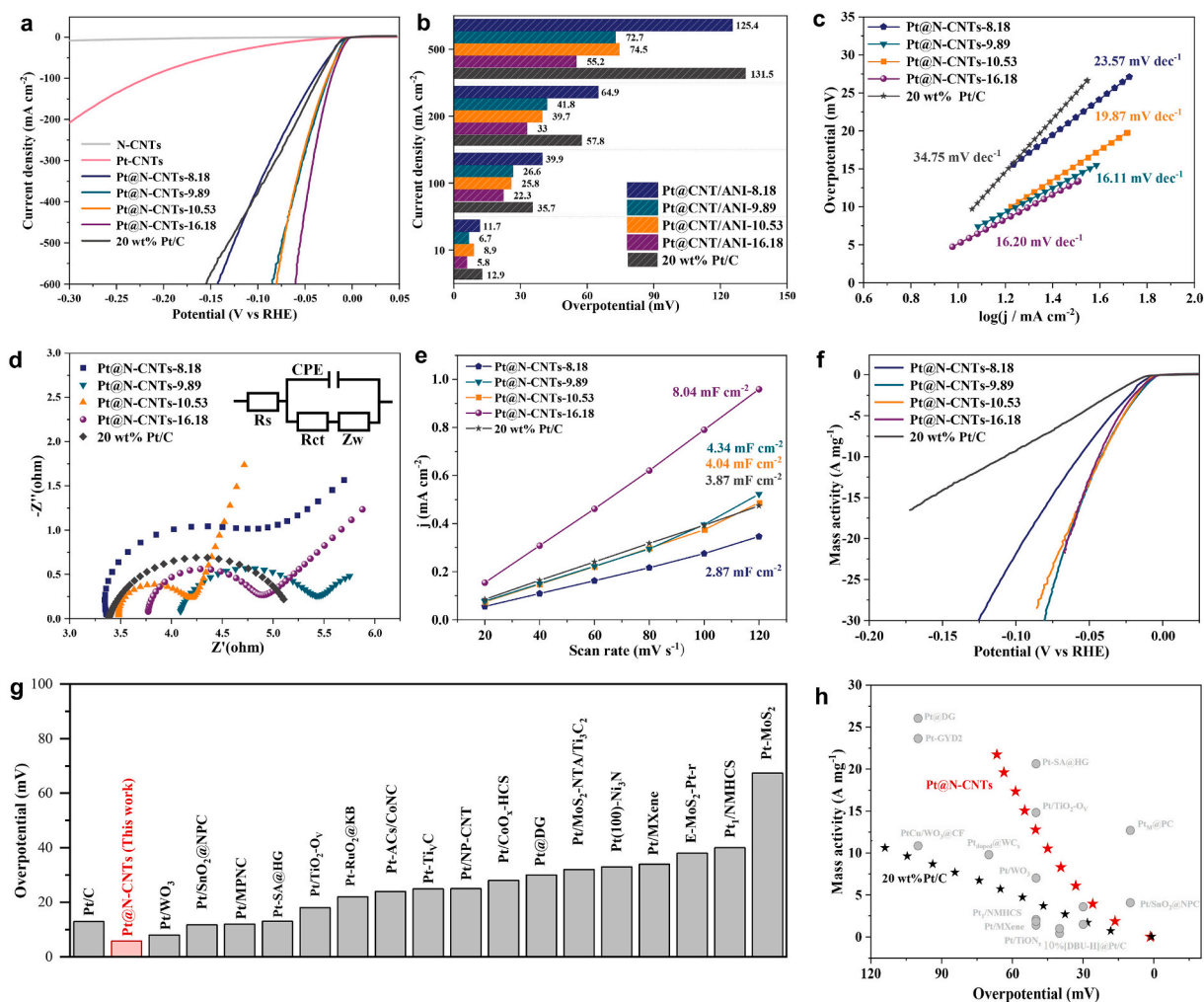
Fig. 4. Electrocatalytic performance. a. LSV curves of N-CNTs, Pt-CNTs, Pt@N-CNTs and 20 wt% Pt/C. **b.** Overpotential at different current densities. **c.** Tafel plots of Pt@N-CNTs and 20 wt% Pt/C. **d.** EIS plots and **e.** corresponding Cdl values. **f.** Mass activities. **g.** Comparison of overpotential at 10 mA cm^{-2} between Pt@N-CNTs and other state-of-the-art electrocatalysts from Table S4. **h.** Mass activities of Pt@N-CNTs, and recently reported Pt-based HER electrocatalysts from Table S5.

investigating the electron/proton transfer occurring at the interface between a catalyst and an electrolyte, providing insights into the electrocatalytic performance [41]. Fig. 4d and Table S2 demonstrate a significant decrease in charge transfer resistance (R_{ct}) for all Pt@N-CNTs catalysts compared to Pt/C, indicating enhanced electron/proton transfer at the interface between Pt@N-CNTs and the electrolyte. This can be attributed to the higher conductivity of CNTs, which enables more efficient electron transport and reduces overpotential compared to amorphous carbon.

Taking the catalyst cost into consideration for practical applications, the mass activities of the catalysts were evaluated by normalizing the LSV curves with the mass of Pt. Fig. 4f illustrates the remarkably high mass activity of Pt@N-CNTs. At an overpotential of 50 mV, the Pt@N-CNTs-8.18 catalyst exhibits a mass activity of 8.32 mA mg^{-1}, which is twice that of commercial Pt/C (4.06 mA mg^{-1}), while the Pt@N-CNTs-16.18 catalyst reaches as high as 12.27 mA mg^{-1}. Furthermore, compared to other advanced Pt-based catalysts, Pt@N-CNTs demonstrates superior mass activity (Fig. 4h). Furthermore, to quantify the catalytic efficiency of individual Pt sites, the turnover frequency (TOF) was calculated by inferring the number of active sites from ECSA. Since the exact number and nature of hydrogen binding sites is not known, we estimated the number of active sites by considering the surface sites on Pt atoms as possible active sites [42]. Table S3 reveals that the TOF values for Pt@N-CNTs at an overpotential of 50 mV are notably superior to those of 20 wt% Pt/C (3.23 s^{-1}). More specifically, the TOF values for

Pt@N-CNTs-8.18, Pt@N-CNTs-9.18, Pt@N-CNTs-10.18, and Pt@N-CNTs-16.18 stand at 3.68, 4.67, 5.32, and 4.05 s^{-1}, respectively. Remarkably, despite a substantially lower Pt loading, Pt@N-CNTs presented superior HER activity in contrast to Pt/C, thus indicating that the anchoring of Pt onto the N-doped carbon support enhances the intrinsic catalytic activity.

3.4. Stability and hydrogen redox flow batteries

Catalyst stability is a crucial parameter for evaluation. The cyclic stability of Pt@N-CNTs and Pt/C was evaluated by comparing the LSV curves before and after 1, 3000, and 5000 cycles in a 1 M HClO$_4$ solution, as illustrated in Fig. 5d. Pt@N-CNTs-16.18 demonstrates remarkable overpotential stability even after 3000 CV cycles, exhibiting an increase of only 2.6 mV at 10 mA cm^{-2}. Additionally, Pt@N-CNTs exhibits minimal variation in overpotential, with a mere 15 mV change after 5000 cycles, even at a large current density of 200 mA cm^{-2}. Fig. S12a presents the TEM image of the Pt@N-CNTs catalyst after cycling, along with the corresponding particle size distribution of Pt nanoparticles. The image clearly shows that there is no agglomeration of Pt nanoparticles and their size remains almost unchanged. This demonstrates the effectiveness of the EMSI in preventing the migration and aggregation of nanoparticles during the electrocatalytic process. Moreover, current-time (i-t) measurements were carried out to assess the durability of Pt@N-CNTs. Fig. 5e shows that the current density of the
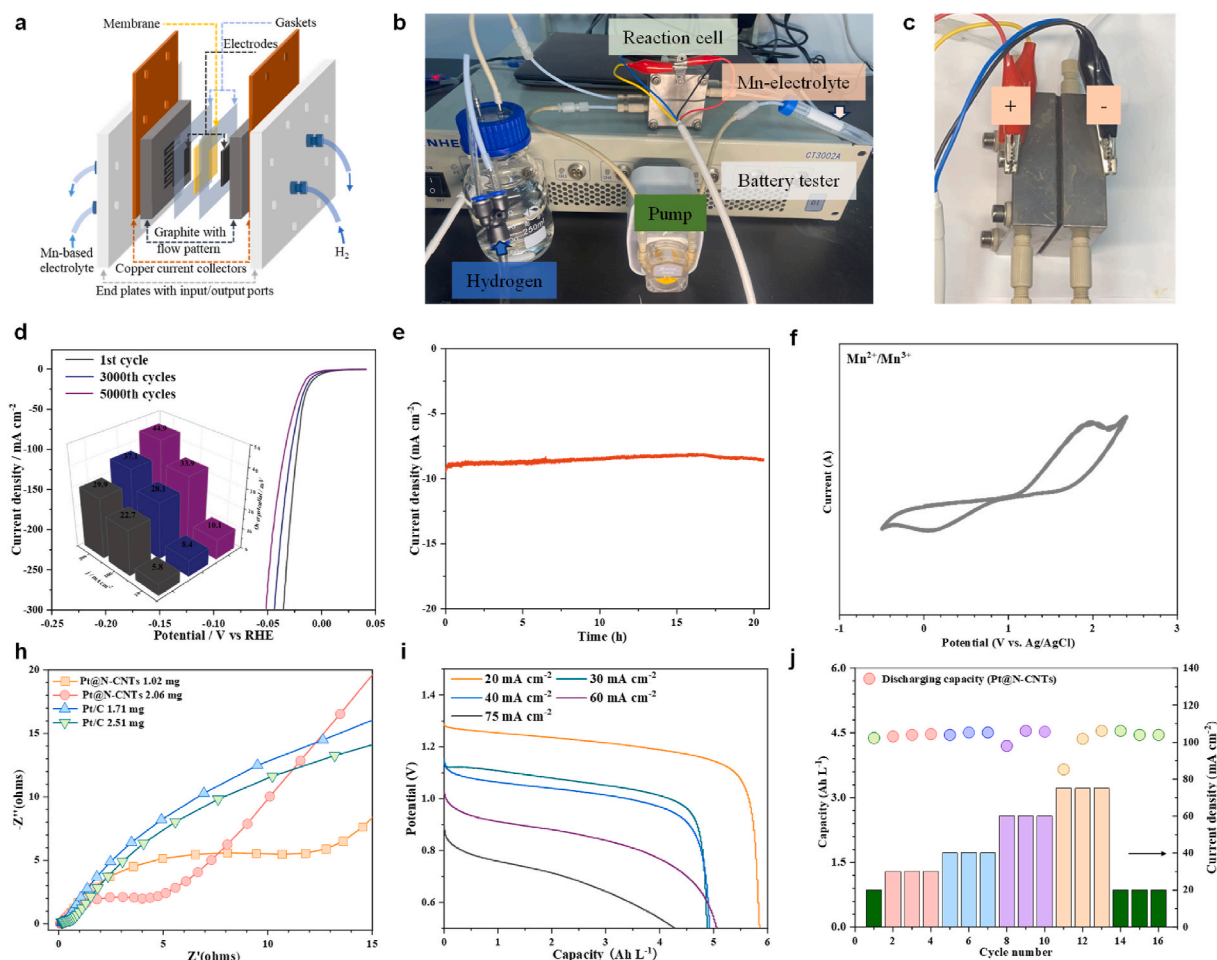
Fig. 5. Stability and application in Mn–H$_2$ battery. a. Schematic structure of Mn–H$_2$ battery system. **b-c.** Photos of a Mn–H$_2$ redox flow battery testing system and a reaction cell. **d.** LSV curves for Pt@N-CNTs before and after 5000 cycles of CV test (Inset: Overpotential at different current densities). **e.** i-t curves of Pt@N-CNTs for 20 h. **f.** CV plot of the Mn–H$_2$ battery. **h.** EIS plots of the Mn–H$_2$ battery. **i.** Discharge curves of the cell under different current densities. **j.** Rate capability of the cell in the electrolyte of soluble Mn^{2+} aqueous.

Pt@N-CNTs catalyst exhibited only a slight decrease after 20 h, indicating its sustained high catalytic activity and stability throughout long-term electrolysis. These findings strongly support the exceptional electrocatalytic stability of Pt@N-CNTs, which can be attributed to the robust π-π interactions among Pt, aniline, and CNTs. Furthermore, the pronounced EMSI effect effectively prevents the aggregation of Pt NPs and promotes substantial electron transfer.

Flow batteries are widely regarded as a promising solution for large-scale energy storage applications due to their advantages of easy scalability, long cycle life, low maintenance cost, fast response and environmental friendliness [43,44]. To further investigate the performance of the Pt@N-CNTs catalyst in practical applications, we utilized it as the anode in a manganese-hydrogen (Mn–H$_2$) flow battery, employing a soluble Mn^{2+} aqueous solution as the electrolyte (Fig. 5a–c, f). In the operational Mn–H$_2$ battery, Mn^{2+} ions in the electrolyte undergo electrochemical reactions to Mn^{3+}-ions without producing a solid MnO$_2$ deposit, while H$_2$ evolution from H$_2$O is driven by highly active Pt@N-CNTs catalyst on the anode and vice versus [45]. Fig. 5h shows the impedance spectra of the hydrogen electrode, revealing lower charge transfer resistance for the Mn–H$_2$ battery compared to Pt/C, even with a lower catalyst loading. This indicates that the Pt@N-CNTs catalyst effectively accelerates electron/proton transfer, enhancing the kinetics of the anode reaction. Additionally, Fig. 5i displays the galvanostatic discharge curves of the Mn–H$_2$ battery under various current densities, illustrating noteworthy discharge platforms across all current densities. Specifically, the Mn–H$_2$ battery exhibited a charging

plateau reaching as high as 1.3V at 20 mA cm^{-2}. Even at 75 mA cm^{-2}, it still remained at 0.9 V. The rate capability of the battery is crucial for practical energy storage applications. Fig. 5j demonstrates that the discharge capacity of the battery remains around 4.5 Ah L^{-1}, even with an increase in discharge current density from 20 mA cm^{-2} to 75 mA cm^{-2}, indicating similar rate performance between the Mn–H$_2$ battery and Pt/C. The Pt@N-CNTs catalyst can be extended to other types of metal-hydrogen flow batteries, as it reduces the H$_2$ overpotential and provides higher current density, thus paving the way for practical applications of metal-hydrogen flow batteries.

4. Conclusions and perspectives

The excellent HER activity of Pt@N-CNTs can be attributed to the following factors. (1) ***Enhanced interfacial interaction***. A strong EMSI effect is formed between Pt NPs and the CNT supports, leading to changes in the charge distribution and surface properties of the catalyst and thereby significantly enhancing its catalytic activity. (2) ***Highly conductive and continuous carbon framework***. CNTs act as carbon supports, offering good stability, conductivity, and confinement effects [46,47]. Their hollow tubular structure with a high specific surface area allows for increased exposure of Pt NPs. Additionally, CNTs can modulate electron spin density and charge redistribution at active sites for the HER by supporting transition metals. (3) ***Incorporation of aniline molecules to enhance the catalyst matrix***. The N atoms in aniline act as strong electron-accepting groups, enhancing the π-π interaction between

Pt, aniline, and CNTs. This further promotes the EMSI effect and optimizes the Gibbs free energy of H adsorption. Furthermore, this strong interaction effectively prevents the migration and aggregation of submicron Pt NPs.

In summary, this study demonstrates a viable metal-support engineering approach to preparing Pt@N-CNTs catalysts with a strong EMSI effect via a facile and simple microwave reduction protocol. The inclusion of N-doped CNT supports enhances the EMSI effect with platinum Pt, effectively impeding the migration and aggregation of ultrafine Pt NPs. Moreover, the charge redistribution optimizes the Gibbs free energy of hydrogen adsorption. The highly dispersed ultrafine Pt NPs with abundant exposed active sites and the hollow tubular structure with efficient electron/mass transfer significantly contribute to the excellent HER activity. The experimental results reveal that Pt@N-CNTs displays remarkable HER activity, surpassing 20 wt% Pt/C and other advanced Pt-based catalysts. The optimized Pt@N-CNTs catalyst exhibits significantly low overpotentials of 5.8 mV and 55.2 mV at current densities of 10 mA cm^{-2} and 500 mA cm^{-2}, respectively. Notably, at an overpotential of 50 mV, Pt@N-CNTs demonstrates a high TOF of 4.05 s^{-1} and a substantial mass activity of 12.72 A mg^{-1}. This study proposes a novel approach for the design and implementation of HER electrocatalysts that can synergize low cost and high activity, thereby enhancing the catalytic performance of water splitting, particularly at high current densities. Of greater significance is the fact that this simple and mild one-step microwave-assisted approach is both faster and more cost-effective in comparison to conventional techniques like sol-gel and electrochemical deposition. Furthermore, it aids in achieving the homogeneous distribution of metal particles, thereby enhancing the catalyst's activity and stability.

CRediT authorship contribution statement

Jinhua Mai: Writing – original draft, Investigation. **Yulong Zhang:** Supervision, Investigation. **Huan He:** Supervision. **Yue Luo:** Investigation. **Xiaoqun Zhou:** Conceptualization. **Kunsong Hu:** Conceptualization. **Gang Liu:** Funding acquisition. **Manoj Krishna Sugumar:** Writing – review & editing. **Chee Tong John Low:** Writing – review & editing, Supervision. **Xinhua Liu:** Writing – review & editing. **Rui Tan:** Writing – review & editing, Conceptualization.

Declaration of competing interest

The authors declare that they have no known competing financial interests or personal relationships that could have appeared to influence the work reported in this paper.

Data availability

Data will be made available on request.

Acknowledgements

Appendix A. Supplementary data

Supplementary data to this article can be found online at https://doi.org/10.1016/j.mtchem.2024.102079.

References

[1] L. Schlapbach, A. Zuttel, Hydrogen-storage materials for mobile applications, Nature 414 (2001) 353–358.

[2] Z. Chen, H. Qing, R. Wang, R. Wu, Charge pumping enabling Co-NC to outperform benchmark Pt catalyst for pH-universal hydrogen evolution reaction, Energy Environ. Sci. 14 (2021) 3160–3173.

[3] T.F. Jaramillo, K.P. Jorgensen, J. Bonde, J.H. Nielsen, S. Horch, I. Chorkendorff, Identification of active edge sites for electrochemical H$_2$ evolution from MoS$_2$ nanocatalysts, Science 317 (2007) 100–102.

[4] B. Fei, Z. Chen, J. Liu, H. Xu, X. Yan, H. Qing, M. Chen, R. Wu, Ultrathinning Nickel sulfide with modulated electron density for efficient water splitting, Adv. Energy Mater. 10 (2020) 2001963.

[5] H. Wu, C. Feng, L. Zhang, J. Zhang, D.P. Wilkinson, Non-noble metal electrocatalysts for the hydrogen evolution reaction in water electrolysis, Electrochem. Energy Rev. 4 (2021) 473–507.

[6] Z. Pu, I.S. Amiinu, R. Cheng, P. Wang, C. Zhang, S. Mu, W. Zhao, F. Su, G. Zhang, S. Liao, S. Sun, Single-atom catalysts for electrochemical hydrogen evolution reaction: Recent Advances and Future Perspectives, Nano-Micro Lett. 12 (2020) 21.

[7] Y. Han, H. Duan, W. Liu, C. Zhou, B. Wang, Q. Jiang, S. Feng, W. Yan, T. Tan, R. Zhang, Engineering the electronic structure of platinum single-atom sites via tailored porous carbon nanofibers for large-scale hydrogen production, Appl. Catal. B Environ. 335 (2023) 122898.

[8] L. Ni, Z. Zhang, Z. Zhao, H. Li, Hierarchical macro-mesoporous electrocatalysts with dual-active sites of Ru single atoms and monodispersed Ru-Mo nanoclusters for efficient hydrogen evolution, Mater. Today Chem. 26 (2022) 101046.

[9] D. Wang, X. Jiang, Z. Lin, X. Zeng, Y. Zhu, Y. Wang, M. Gong, Y. Tang, G. Fu, Ethanol-induced hydrogen Insertion in ultrafine IrPdH Boosts pH-universal hydrogen evolution, Small 18 (2022) 2204063.

[10] Y. Wu, W. Wei, R. Yu, L. Xia, X. Hong, J. Zhu, J. Li, L. Lv, W. Chen, Y. Zhao, L. Zhou, L. Mai, Anchoring sub-Nanometer Pt clusters on Crumpled paper-like MXene enables high hydrogen evolution mass activity, Adv. Funct. Mater. 32 (2022) e2110910.

[11] Y. Zhao, P.V. Kumar, X. Tan, X. Lu, X. Zhu, J. Jiang, J. Pan, S. Xi, H.Y. Yang, Z. Ma, T. Wan, D. Chu, W. Jiang, S.C. Smith, R. Amal, Z. Han, X. Lu, Modulating Pt-O-Pt atomic clusters with isolated cobalt atoms for enhanced hydrogen evolution catalysis, Nat. Commun. 13 (2022) 2430.

[12] J. Ding, X. Jiang, C. Wang, Z. Zhu, C. Xu, Y. Zhou, X. Wang, Q. Liu, Z. Liu, Y. Tang, J. Lin, G. Fu, Epitaxial growth triggered core-shell Pd@RuP nanorods for high-efficiency electrocatalytic hydrogen evolution, J. Energy Chem. 86 (2023) 510–517.

[13] C. Li, J. Baek, Recent Advances in noble metal (Pt, Ru, and Ir)-Based electrocatalysts for efficient hydrogen evolution reaction, ACS Omega 5 (2020) 31–40.

[14] W. Yang, S. Zhang, Q. Chen, C. Zhang, Y. Wei, H. Jiang, Y. Lin, M. Zhao, Q. He, X. Wang, Y. Du, L. Song, S. Yang, A. Nie, X. Zou, Y. Gong, Conversion of Intercalated MoO$_3$ to Multi-Heteroatoms-doped MoS$_2$ with high hydrogen evolution activity, Adv. Mater. 32 (2020) e2001167.

[15] R.M.S. Yoo, A. Djire, Decoupling the surface and Bulk Reactivities of MXenes and catalytic activity tuning through surface Chemistry modification, ACS Catal. 13 (2023) 6823–6836.

[16] S. Liang, H. Hu, J. Liu, H. Shen, Q. Li, N. Qiu, H. Guo, X. Guo, S. Du, Y. Zhu, J. Liu, J.P. Attfield, M. Yang, Nickel-nitride composite: an eco-friendly and efficient alternative to platinum for electrocatalytic hydrogen production, Appl. Catal. B Environ. 337 (2023) 123008.

[17] X. Wang, X. Zhang, Y. Xu, H. Song, X. Min, Z. Tang, C. Pi, J. Li, B. Gao, Y. Zheng, X. Peng, P.K. Chu, K. Huo, Heterojunction Mo-based binary and ternary nitride catalysts with Pt-like activity for the hydrogen evolution reaction, Chem. Eng. J. 470 (2023) 144370.

[18] W. Xu, R. Zhao, Q. Li, B. Sun, J. Wu, W. Zhong, Y. Gao, X. Nan, Q. Huang, Y. Yang, X. Li, N. Yang, Q. Zhang, Overall water splitting on the NiS/NiS$_2$ heterostructures Featuring Self-Equilibrium orbital Occupancy, Adv. Energy Mater. 13 (2023) 2300978.

[19] P. Fang, M. Zhu, J. Liu, Z. Zhu, J. Hu, X. Xu, Making ternary-metal Hydroxysulfide catalyst via cathodic Reconstruction with ion regulation for industrial-Level hydrogen Generation, Adv. Energy Mater. 13 (2023) 2301222.

[20] K. Feng, R. Song, J. Xu, Y. Chen, C. Lu, Y. Li, W. Hofer, H. Lin, Z. Kang, J. Zhong, The S-Fe(Ni) sub-surface active sites for efficient and stable overall water splitting, Appl. Catal. B Environ. 325 (2023) 122365.

[21] J. Chi, L. Guo, J. Mao, T. Cui, J. Zhu, Y. Xia, J. Lai, L. Wang, Modulation of electron structure and Dehydrogenation kinetics of Nickel phosphide for Hydrazine-assisted Self-Powered hydrogen production in seawater, Adv. Funct. Mater. (2023) 2300625.

[22] S. Lv, Y. Deng, Q. Liu, Z. Fu, X. Liu, M. Wang, Z. Xiao, B. Li, L. Wang, Carbon-quantum-dots-involved Fe/Co/Ni phosphide open nanotubes for high effective seawater electrocatalytic decomposition, Appl. Catal. B Environ. 326 (2023) 122403.

[23] G. Ma, J. Ye, M. Qin, T. Sun, W. Tan, Z. Fan, L. Huang, X. Xin, Mn-doped NiCoP nanopin arrays as high-performance bifunctional electrocatalysts for sustainable hydrogen production via overall water splitting, Nano Energy 115 (2023) 108679.

[24] K.L. Zhou, Z. Wang, C.B. Han, X. Ke, C. Wang, Y. Jin, Q. Zhang, J. Liu, H. Wang, H. Yan, Platinum single-atom catalyst coupled with transition metal/metal oxide heterostructure for accelerating alkaline hydrogen evolution reaction, Nat. Commun. 12 (2021) 3783.

[25] A. Mosallanezhad, C. Wei, P. Ahmadian Koudakan, Y. Fang, S. Niu, Z. Bian, B. Liu, T. Huang, H. Pan, G. Wang, Interfacial synergies between single-atomic Pt and CoS for enhancing hydrogen evolution reaction catalysis, Appl. Catal. B Environ. 315 (2022) 121534.

[26] F. Li, D.H. Kweon, G. Han, H. Noh, W. Che, I. Ahmad, H.Y. Jeong, Z. Fu, Y. Lu, J. Baek, Merging platinum single atoms to achieve Ultrahigh mass activity and low hydrogen production cost, ACS Nano 17 (2023) 2923–2931.

[27] F. Guo, T.J. Macdonald, A.J. Sobrido, L. Liu, J. Feng, G. He, Recent Advances in ultralow-Pt-loading electrocatalysts for the efficient hydrogen evolution, Adv. Sci. 10 (2023) 2301098.

[28] R. Zhang, Y. Li, X. Zhou, A. Yu, Q. Huang, T. Xu, L. Zhu, P. Peng, S. Song, L. Echegoyen, F. Li, Single-atomic platinum on fullerene C_{60} surfaces for accelerated alkaline hydrogen evolution, Nat. Commun. 14 (2023).

[29] N. Acerbi, S.C.E. Tsang, G. Jones, S. Golunski, P. Collier, Rationalization of interactions in Precious metal/Ceria catalysts using the d-band center Model, Angew. Chem. Int. Ed. 52 (2013) 7737–7741.

[30] Q. Zhu, J. Li, Q. Xu, Immobilizing metal nanoparticles to metal-Organic frameworks with size and Location Control for optimizing catalytic performance, J. Am. Chem. Soc. 135 (2013) 10210–10213.

[31] H. Wang, X.K. Gu, X. Zheng, H. Pan, J. Zhu, S. Chen, L. Cao, W.X. Li, J. Lu, Disentangling the size-dependent geometric and electronic effects of palladium nanocatalysts beyond selectivity, Sci. Adv. 5 (2019) eaat6413.

[32] Z. Li, S. Ji, Y. Liu, X. Cao, S. Tian, Y. Chen, Z. Niu, Y. Li, Well-defined materials for Heterogeneous catalysis: from nanoparticles to isolated single-atom sites, Chem. Rev. 120 (2020) 623–682.

[33] L. Liu, A. Corma, Metal catalysts for Heterogeneous catalysis: from single atoms to nanoclusters and nanoparticles, Chem. Rev. 118 (2018) 4981–5079.

[34] D. Liu, Q. He, S. Ding, L. Song, Structural regulation and support coupling effect of single-atom catalysts for Heterogeneous catalysis, Adv. Energy Mater. 10 (2020) 2001482.

[35] X.K. Wan, H.B. Wu, B.Y. Guan, D. Luan, X.W.D. Lou, Confining sub-Nanometer Pt clusters in hollow mesoporous carbon Spheres for Boosting hydrogen evolution activity, Adv. Mater. 32 (2020) 19011349.

[36] J. Chen, Y. Ha, R. Wang, Y. Liu, H. Xu, B. Shang, R. Wu, H. Pan, Inner Co synergizing outer Ru supported on carbon nanotubes for efficient pH-universal hydrogen evolution catalysis, Nano-Micro Lett. 14 (2022) e186.

[37] P. Kuang, Y. Wang, B. Zhu, F. Xia, C.W. Tung, J. Wu, H.M. Chen, J. Yu, Pt single atoms supported on N-doped mesoporous hollow carbon Spheres with enhanced electrocatalytic H_2-evolution activity, Adv. Mater. 33 (2021) e2008599.

[38] J. Guo, J. Huo, Y. Liu, W. Wu, Y. Wang, M. Wu, H. Liu, G. Wang, Nitrogen-doped porous carbon supported Nonprecious metal single-atom electrocatalysts: from synthesis to application, Small Methods 3 (2019) 1900159.

[39] Y. Jiang, Y. Lu, X. Lv, D. Han, Q. Zhang, L. Niu, W. Chen, Enhanced catalytic performance of Pt-free Iron Phthalocyanine by Graphene support for efficient oxygen reduction reaction, ACS Catal. 3 (2013) 1263–1271.

[40] Y. Zhang, X. Fan, J. Jian, D. Yu, Z. Zhang, L. Dai, A general polymer-assisted strategy enables unexpected efficient metal-free oxygen-evolution catalysis on pure carbon nanotubes, Energy Environ. Sci. 10 (2017) 2312–2317.

[41] M.B. Stevens, L.J. Enman, A.S. Batchellor, M.R. Cosby, A.E. Vise, C.D.M. Trang, S. W. Boettcher, Measurement techniques for the study of Thin Film Heterogeneous water oxidation electrocatalysts, Chem. Mater. 29 (2017) 120–140.

[42] J. Kibsgaard, T.F. Jaramillo, Molybdenum Phosphosulfide: an active, acid-stable, Earth-abundant catalyst for the hydrogen evolution reaction, Angew. Chem. Int. Ed. 53 (2014) 14433–14437.

[43] W. Chen, G. Li, A. Pei, Y. Li, L. Liao, H. Wang, J. Wan, Z. Liang, G. Chen, H. Zhang, J. Wang, Y. Cui, A manganese-hydrogen battery with potential for grid-scale energy storage, Nat. Energy 3 (2018) 428–435.

[44] R. Tan, A. Wang, R. Malpass-Evans, R. Williams, E.W. Zhao, T. Liu, C. Ye, X. Zhou, B.P. Darwich, Z. Fan, L. Turcani, E. Jackson, L. Chen, S.Y. Chong, T. Li, K.E. Jelfs, A.I. Cooper, N.P. Brandon, C.P. Grey, N.B. McKeown, Q. Song, Hydrophilic microporous membranes for selective ion separation and flow-battery energy storage, Nat. Mater. 19 (2020) 195–202.

[45] J. Rubio-Garcia, A. Kucernak, D. Zhao, D. Li, K. Fahy, V. Yufit, N. Brandon, M. Gomez-Gonzalez, Hydrogen/manganese hybrid redox flow battery, JPhys Energy 1 (2019) 15006.

[46] Y. Zheng, Y. Jiao, Y. Zhu, L.H. Li, Y. Han, Y. Chen, M. Jaroniec, S. Qiao, High electrocatalytic hydrogen evolution activity of an Anomalous Ruthenium catalyst, J. Am. Chem. Soc. 138 (2016) 16174–16181.

[47] S. Nong, W. Dong, J. Yin, B. Dong, Y. Lu, X. Yuan, X. Wang, K. Bu, M. Chen, S. Jiang, L. Liu, M. Sui, F. Huang, Well-dispersed Ruthenium in mesoporous crystal TiO$_2$ as an advanced electrocatalyst for hydrogen evolution reaction, J. Am. Chem. Soc. 140 (2018) 5719–5727.